PHYSICAL REVIEW E **108**, 024135 (2023)

Random walks on modular chains: Detecting structure through statistics

Matthew Gerry [1] and Dvira Segal [1,2,*]
[1]*Department of Physics, University of Toronto, 60 Saint George St., Toronto, Ontario M5S 1A7, Canada*
[2]*Chemical Physics Theory Group, Department of Chemistry and Centre for Quantum Information and Quantum Control, University of Toronto, 80 Saint George St., Toronto, Ontario M5S 3H6, Canada*

(Received 17 May 2023; accepted 4 August 2023; published 22 August 2023)

We study kinetic transport through one-dimensional modular networks consisting of alternating domains using both analytical and numerical methods. We demonstrate that the mean velocity is *insensitive* to the local structure of the network, and it depends only on global, structural-averaged properties. However, by examining high-order cumulants characterizing the kinetics, we reveal information on the degree of inhomogeneity of blocks and the size of repeating units in the network. Specifically, in *unbiased* diffusion, the kurtosis is the first transport coefficient that exposes structural information, whereas in *biased* chains, the diffusion coefficient already reveals structural motifs. Nevertheless, this latter dependence is weak, and it disappears at both low and high biasing. Our study demonstrates that high-order moments of the population distribution over sites provide information about the network structure that is not captured by the first moment (mean velocity) alone. These results are useful towards deciphering mechanisms and determining architectures underlying long-range charge transport in biomolecules and biological and chemical reaction networks.

DOI: 10.1103/PhysRevE.108.024135

I. INTRODUCTION

Rolf Landauer's famous saying that "the noise is the signal" [1] was originally stated in the context of noise measurements in electronic conductors, which can be used to reveal underlying many-electron interactions in the device. However, whether concerned with electronic, chemical, or biological kinetics, this statement captures a profound observation: That fluctuations of a signal can be used to probe the system—and more fundamentally so than the mean signal alone [2]. Considering, for example, charge transport in conductors: The probably distribution function (PDF) to transfer n electrons within a certain time encapsulates the full information on the charge current and its moments [3,4]. Similarly, the PDF for first passage processes, e.g., in the context of protein folding or transport through ion channels, contains rich information beyond what is conveyed by the averaged measure of the mean first-passage time [5].

Chemical and biological reactions can be coarse-grained and modeled as network systems, and general principles can be understood by studying such systems in the context of stochastic thermodynamics [6–9]. The structure and topology of these networks can, for instance, be detected from the PDF of first-passage processes [10–13]. In particular, in chemical kinetics, details on reaction mechanisms can be inferred from the statistics of the kinetics. It was shown in Ref. [14] that fluctuations in the time to complete an enzymatic cycle can be used to bound the number of intermediate steps. Recent studies continued and interrogated higher-order moments of the PDF of the cycle completion time, beyond the mean and the variance. They found that the skewness and kurtosis of this PDF reveal, e.g., whether the enzymatic network was unicyclic or multicyclic, information that was not reflected in the second moment of the PDF [15,16]. Investigations into the statistics of observable currents at steady state in systems described by kinetic networks have also revealed bounds on the relative fluctuations of the current determined explicitly by network structure [17,18].

In a different context, shot noise measurements of mesoscale, nanoscale, and atomic conductors provide information on quantum transport that cannot be resolved from the electrical conductance itself [19]. As such, shot noise experiments were used to characterize, e.g., the fractional quantum Hall effect [20], electron transport in the Kondo regime [21], electron-phonon interaction effects in molecular junctions [22,23], and structural and energetic asymmetry of atomic-scale conductors [24]. Beyond shot noise, which corresponds to the second moment of carriers flow, it was recently shown that the skewness and kurtosis of the PDF of charge transport reveal information on the violation of the thermodynamic uncertainty relation (TUR) [25,26] and the impact of many-body effects in transport [27].

The objective of this study is to identify what new, detailed information on the structure of a kinetic network can be revealed from successive high moments of the distribution of population, beyond its mean. We focus on random walks on one-dimensional chains, which are either homogeneous or modular, and relate these chains to finite unicyclic networks. We note that in doing so, we do not address the question of how unicyclic vs multicyclic network structure may be distinguished through transport statistics.

An example of a modular system is depicted in Fig. 1; the configurational space map of the model is presented in Fig. 2.

---

[*] dvira.segal@utoronto.ca

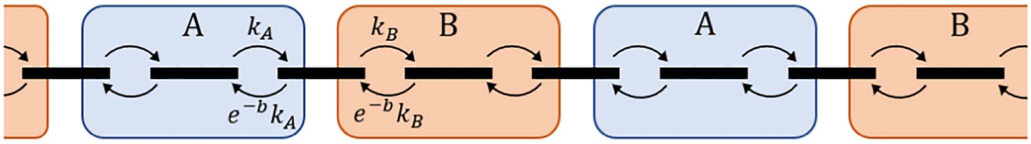

FIG. 1. Diagram of a modular chain on which an infinite random walk plays out. The unions of segments labeled "A" and "B" make up regions A and B, respectively, where forward and reverse rates are given by Eqs. (1) and (2). For the example shown here the number of sites in each segment is $m_A = m_B = 2$.

It was previously shown, through numerical simulations of quantum dissipative transport, that the average electron current through modular junctions depends only on the *average* resistance of the chain, and it is insensitive to the local structure [28]. These results were demonstrated numerically using two approaches, Büttiker probes simulations [29] and quantum rate equations of the Lindblad form. One of the goals of the present study is to derive an analogous result analytically, which we do using classical kinetics for modular networks with unit block size. More generally, our aim here is to reveal with analytical and numerical work information about the local structure of a network (e.g., inhomogeneity of blocks and size of repeating units) from cumulants of the distribution (mean, diffusion coefficient, skewness, and kurtosis).

We discover that in an *unbiased* random walk on a modular network, the kurtosis is the *first* cumulant that expresses local structural information. In contrast, in *biased* random walks, the diffusion coefficient can reveal structural information, but this dependence is rather weak. The sensitivity to the local structure amplifies only in the skewness and more so in the kurtosis.

The paper is organized as follows. We present the random walk models, in real space and configuration space, in Sec. II. We study the statistics of carriers transport in Sec. III. Analytic results for the first four cumulants of the population distribution for modular chains with a block size one are presented in Secs. III A and III B. Complementing this analysis, numerical simulations are included in Sec. III C. Real-space simulations of the random walk are presented in Sec. IV, revealing the rich structure of the PDF in modular models. We discuss our results and conclude in Sec. V.

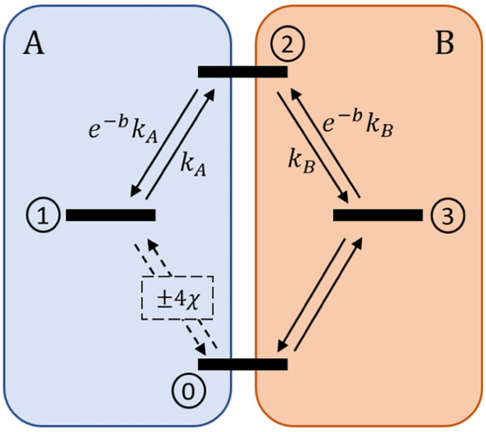

FIG. 2. The modular chain of Fig. 1 can be mapped into a a finite cyclic network of states. This cyclic network is created by recognizing the periodicity in the structure of the modular infinite chain. The clockwise direction around the cycle corresponds to the forward direction of the random walk. Full counting statistics tracks the net number of times the system completes the $0 \rightarrow 1$ transition, as indicated by the dashed arrows and counting field. This number is then scaled up by $m_P = 4$ to count the number of steps "away" from the initial site at steady state.

II. MODELS

We study random walks in structured networks corresponding to two setups: (1) An infinite one-dimensional modular lattice with repeating segments (Fig. 1) and (2) a finite unicyclic network (Fig. 2) representing reaction kinetics. Alternatively, the cyclic model corresponds to the configurational space of the infinite chain model (1). These models help to highlight the effects of underlying periodic and nontrivial structure, which have been investigated in numerous past works for random walks as well as diffusion in continuous space explored using Langevin or Fokker-Planck simulations [30–38].

A. Modular and homogeneous chains

We consider a continuous-time random walk on an infinite modular chain; see Fig. 1. In our model transition rates alternate between different values for segments some number of sites long. Most generally, segments associated with the two sets of transition rates are m_A and m_B sites long, where m_A and m_B may or may not be equal. The total period for this alternation of transition rates is then $m_P = m_A + m_B$. The blocks are made distinct by using different hoping rates between sites within segment A and within segment B.

This network can represent a polymer with alternating units, stiff and flexible. Such modular structures may be used to model long-range charge transport in polymers and biomolecules [39–41]. One such example pertains to the nearest-neighbor hopping model for charge transport in DNA, wherein an alternating structure for the hopping rates can be established via the sequence of base pairs [42].

The object of our calculation is the PDF to find the system n sites away from its starting point, within some time. We refer to the first four cumulants of this PDF, scaled by time, as the mean velocity, diffusion coefficient, skewness, and kurtosis.

The forward transition rate from site i to site $i+1$ is given by

$$k_{i+1,i} = \begin{cases} k_A \equiv \frac{\tau^2}{\gamma_A}, & (i \bmod m_P) < m_A \\ k_B \equiv \frac{\tau^2}{\gamma_B}, & (i \bmod m_P) \geqslant m_A. \end{cases} \qquad (1)$$

Here we apply the modulo (mod) operation. We note here that we start the site-counting at zero, which is an A-type site, and that there is a site for every $i \in \mathbb{Z}$. τ is a constant which gives rise to an overall scale for the rates. The rates differ due to the difference in the values of γ_A and γ_B, which serve a function analogous to resistance.

Note that in the corresponding quantum transport model [28], blocks A and B were made distinct by setting different local decoherence rates for electrons, being high or low relative to the tunneling energies τ. A segment with high (low) decoherence corresponds to a flexible (rigid) region in a polymer [43,44].

Assuming local detailed balance, given the forward transition rates, the reverse rates are given by

$$k_{i,i+1} = e^{-b} k_{i+1,i}, \tag{2}$$

where b represents a uniform bias. In the context of a charged particle hopping under an external electric field, the bias is $b = \Delta\mu/(k_B T)$, with $\Delta\mu$ the local potential bias, T the temperature, and k_B the Boltzmann constant. Each individual transition is symmetric in the case that $b = 0$, and the walk is biased in the forward direction for $b > 0$. In what follows we assume the bias is equal between every pair of neighboring sites.

To contrast the modular chain, we build a corresponding homogeneous chain whose forward transition rate at all sites is given by $k^* = \tau^2/\gamma^*$, with $\gamma^* \equiv (m_A\gamma_A + m_B\gamma_B)/m_P$ (the average of γ_A and γ_B weighted by their respective segment lengths). The reverse rate is uniformly given by this rate scaled by e^{-b}, in analogy to the above.

We will focus primarily on the case that the segment lengths are equal, $m_A = m_B \equiv m$ such that $m_P = 2m$. Accordingly, k^* is calculated simply using the arithmetic mean value, $\gamma^* = \bar{\gamma} = (\gamma_A + \gamma_B)/2$; $k^* = \tau^2/\bar{\gamma}$.

B. Bipartite finite cycle

In addition to the infinite modular chain and its associated homogeneous counterpart, we consider a closely related *finite* network consisting of a single cycle with m_P sites; see Fig. 2. This cyclic kinetic network can be viewed as a reaction network with a total of m_P internal states: The first m_A steps are slow, and they are followed by m_B fast steps. At the end of each kinetic cycle, a product specie is generated, and thus the completion of a cycle can be monitored. The probability distribution for the diffusion process along the chain now describes the statistics of the number of product molecules formed.

Furthermore, the finite cycle can be constructed from the infinite chain discussed in Sec. II A by connecting the rightmost site of a "B" segment back to the leftmost site of the previous "A" segment. The transition rates on this cyclic network can be defined in accord using Eqs. (1) and (2), but replacing each index i with (i mod m_P), such that neither ever exceeds $m_P - 1$, but instead cycles back to 0. For example, if $m = 2$ ($m_P = 4$), the unicyclic network we associate with the random walk consists of four states (labeled $i = 0, 1, 2, 3$, as shown in Fig. 2), with $k_{1,0} = k_{2,1} = k_A$, $k_{3,2} = k_{0,3} = k_B$, and reverse rates equal to these forward rates scaled by e^{-b}. $k_{i,j} = 0$ for any $|i - j| \geqslant 2$, with the exception of the last-to-first transition closing the loop. For comparison, we also study the associated homogeneous cycle by setting all forward rates to k^*.

We build the random walk on the cyclic network using exactly the same transition rates as one on the infinite modular chain. As a result, the statistics of the net number of steps taken in the clockwise direction follows the exact same statistics as the net number of steps taken on the corresponding infinite chain. We use the variable n to represent both of these quantities.

The main objective of this work is to investigate how signatures of modular structure, in comparison to the homogeneous structure, manifest in the statistics of random walks on these chains, at steady state. Useful information on the structure that we would like to reveal is (1) the degree of inhomogeneity, $\Delta\gamma = \gamma_A - \gamma_B$ and (2) the block size.

III. FULL COUNTING STATISTICS FOR FORWARD STEPS

We are interested in the scaled cumulants for the distribution over n in the long-time limit,

$$\mathcal{C}_k \equiv \lim_{t\to\infty} \frac{\langle\langle n^k(t)\rangle\rangle}{t}, \tag{3}$$

where $n(t)$ is the stochastic variable representing the site of the walker at time t, such that $\langle\langle n^k(t)\rangle\rangle$ is the kth cumulant of the distribution over this quantity. We may suppose $n(0) = 0$, though for large enough t the initial conditions have no impact on the scaled cumulants.

Our implementation of full counting statistics is based on the equivalence between the statistics of n for both the infinite modular chain and the finite cycle introduced in Sec. II. This equivalence arises from the periodicity of the modular structure. Whether we are ultimately interested in the infinite chain or the finite cycle, we carry out full counting statistics by writing down the $m_P \times m_P$ rate matrix, $\mathcal{L}$, for the m_P-state unicyclic network. The off-diagonal elements $\mathcal{L}_{ij}$ are the transition rates $k_{i,j}$ and the diagonal elements are set such that the columns sum to zero [2].

Knowledge of the matrix elements of $\mathcal{L}$ allows us write the rate of change of the probability $\mathcal{P}_i(\mathcal{N};t)$ for the system to be found at site i, given that it has completed exactly $\mathcal{N}$ rounds around the cycle. We choose to register trips around the cycle at the $0 \leftrightarrow 1$ transition, such that [45]

$$\begin{aligned}
\frac{d}{dt}\mathcal{P}_0(\mathcal{N};t) &= -\mathcal{P}_0(\mathcal{N};t)(k_{1,0} + k_{m_P-1,0})\\
&\quad + \mathcal{P}_{m_P-1}(\mathcal{N};t)k_{0,m_P-1}\\
&\quad + \mathcal{P}_1(\mathcal{N}+1;t)k_{0,1},\\
\frac{d}{dt}\mathcal{P}_1(\mathcal{N};t) &= -\mathcal{P}_1(\mathcal{N};t)(k_{0,1} + k_{2,1})\\
&\quad + \mathcal{P}_0(\mathcal{N}-1;t)k_{1,0}\\
&\quad + \mathcal{P}_2(\mathcal{N};t)k_{1,2},\\
\frac{d}{dt}\mathcal{P}_j(\mathcal{N};t) &= -\mathcal{P}_j(\mathcal{N};t)(k_{j\oplus1,j} + k_{j\ominus1,j})\\
&\quad + \mathcal{P}_{j\ominus1}(\mathcal{N};t)k_{j,j\ominus1}\\
&\quad + \mathcal{P}_{j\oplus1}(\mathcal{N};t)k_{j,j\oplus1},
\end{aligned} \tag{4}$$

where the last equation applies to the case where $j \neq 0, 1$, and $\oplus$ and $\ominus$ represent addition and subtraction modulo m_P, respectively.

We then introduce a counting field χ and Fourier transform these quantities with respect to $\mathcal{N}$, leading to the m_P-element characteristic function $\mathcal{Z}(\chi;t)$, whose elements are given by

$$\mathcal{Z}_j(\chi;t) = \sum_{\mathcal{N}=-\infty}^{\infty} \mathcal{P}_j(\mathcal{N};t) e^{i m_P \mathcal{N} \chi}. \tag{5}$$

We include a factor of m_P in the exponent so that the counting effectively tracks the number, n, of forward steps, rather than the number, $\mathcal{N}$, of complete cycles. At sufficiently long times, $n \approx m_P \mathcal{N}$. Getting a χ-dressed (or "tilted") rate matrix, $\mathcal{L}(\chi)$, to time evolve $\mathcal{Z}(\chi;t)$ directly, amounts to multiplying the transition rate $k_{1,0}$ as it appears in $\mathcal{L}$ by a factor $\exp(i m_P \chi)$, and multiplying $k_{0,1}$ by the reciprocal, $\exp(-i m_P \chi)$ [3]. Note that an alternative approach towards obtaining $\mathcal{L}(\chi)$ would be to multiply *every* clockwise transition rate in $\mathcal{L}$ by a factor of just $\exp(i\chi)$ and *every* anticlockwise transition rate by a factor of $\exp(-i\chi)$; for full counting statistics of n in the transient regime this would give greater detail, but it is equivalent at steady state.

The scaled cumulant generating function is given by [45]

$$\mathcal{G}(\chi) = \lim_{t\to\infty} \frac{1}{t} \ln \sum_j \mathcal{Z}_j(\chi;t). \tag{6}$$

This is equivalent to the "dominant" eigenvalue of $\mathcal{L}(\chi)$: That whose real part approaches zero in the limit that χ approaches zero. This function may be used to derive all of the scaled cumulants at steady state via the relation [3],

$$\mathcal{C}_k = \frac{d^k}{d(i\chi)^k} \mathcal{G}(\chi) \bigg|_{\chi=0}. \tag{7}$$

As such, the method outlined above is sufficient to fully characterize the steady-state probability distribution for walkers through systems modeled by the type of modular random walk we have introduced.

A. Analytic results for $m_P = 2$

We focus here on the special case of the modular chain where $m = 1$ (i.e., all segments are one site long and the total spatial period is $m_P = 2$). The differing rates for the two regions are based on differing values of γ_A and γ_B. Without any significant loss of generality, we may suppose $\gamma_A \geqslant \gamma_B$. We want to investigate the statistics of this random walk at steady state, with particular focus on how the values of the scaled cumulants depend on $\Delta\gamma = \gamma_A - \gamma_B$. The limit $\Delta\gamma \to 0$ represents the case where the modular chain becomes identical to its homogeneous counterpart.

The counting field-dependent rate matrix for the cyclic network associated with this modular random walk is

$$\mathcal{L}(\chi) = \begin{pmatrix} -k_A - e^{-b}k_B & e^{-b-2i\chi}k_A + k_B \\ e^{2i\chi}k_A + e^{-b}k_B & -e^{-b}k_A - k_B \end{pmatrix}. \tag{8}$$

Note that setting $m = 1$ gives rise to the special case where two consecutive forward steps of the random walk correspond to two transitions between the *same* pair of states in the finite network. Accordingly, the elements of $\mathcal{L}$ contain sums of two transition rates.

Following the method outlined in Sec. III, we obtain the scaled CGF,

$$\mathcal{G}(\chi) = 2\frac{\tau^2}{\bar{\gamma}} e^{-\frac{b}{2}} \frac{\sqrt{\cosh^2\left(\frac{b}{2} + i\chi\right) - \frac{1}{4}\left(\frac{\Delta\gamma}{\bar{\gamma}}\right)^2 \sinh(i\chi)\sinh(b + i\chi)} - \cosh\left(\frac{b}{2}\right)}{1 - \frac{1}{4}\left(\frac{\Delta\gamma}{\bar{\gamma}}\right)^2}. \tag{9}$$

We remind the reader that the random walk is defined in terms of the rates $k_A = \frac{\tau^2}{\gamma_A}$ and $k_B = \frac{\tau^2}{\gamma_B}$ with the structural asymmetry $\Delta\gamma = \gamma_A - \gamma_B$, further defining the averaged measure for resistance $\bar{\gamma} = \frac{\gamma_A + \gamma_B}{2}$, and the corresponding rate constant, $k^* = \frac{\tau^2}{\bar{\gamma}}$.

1. Mean velocity

Taking the first derivative of $\mathcal{G}(\chi)$ and setting $\chi = 0$, we obtain an expression for the first cumulant, the mean velocity, at steady state,

$$\mathcal{C}_1 = 2\frac{\tau^2}{\bar{\gamma}} e^{-\frac{b}{2}} \sinh\left(\frac{b}{2}\right) = 2e^{-\frac{b}{2}} \sinh\left(\frac{b}{2}\right) k^*. \tag{10}$$

Upon inspection, we note immediately that this quantity is completely independent of the difference $\Delta\gamma$ and is therefore the same for a random walk on the modular chain as it is for the homogeneous chain with the appropriately defined rate k^*. In fact, using the results of Ref. [31], this form of the mean velocity can be derived for the modular random walks considered in this work, independent of the spatial period m_P, as long as $m_A = m_B$. We stress that an experimental investigation of a system modeled by such a random walk *cannot detect the underlying modular structure in any way if it takes into consideration only the first cumulant*.

Checking the limits of high and low b, we see expected behavior. Namely, for small bias b, a linear response behavior shows, $\mathcal{C}_1 \to k^* b$, which goes strictly to zero when $b = 0$. For large b, reverse transitions are suppressed and $\mathcal{C}_1 \to k^*$, which is the forward rate for the homogeneous chain. These trends are displayed in Fig. 3 for modular chains of varying periods $m_P \geqslant 2$ based on numerical simulations.

2. Diffusion coefficient

Following the same procedure but taking the second order derivative, we get an expression for the second cumulant, or

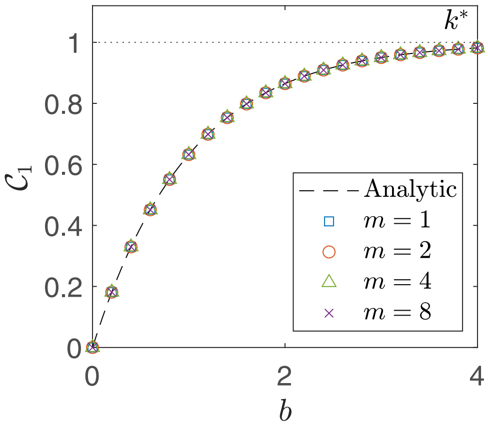

FIG. 3. The first cumulant of the random walk process, corresponding to the mean velocity, presented as a function of the bias b for varying segment lengths, with $m_A = m_B \equiv m$ such that $m_P = 2m$. The dashed curve represents the expression given in Eq. (10). $\tau = \bar{\gamma} = \Delta\gamma = 1$.

the diffusion coefficient,

$$\mathcal{C}_2 = 2\frac{\tau^2}{\bar{\gamma}}\frac{e^{-\frac{b}{2}}}{\cosh\left(\frac{b}{2}\right)}\left[\cosh^2\left(\frac{b}{2}\right) + \frac{1}{4}\sinh^2\left(\frac{b}{2}\right)\left(\frac{\Delta\gamma}{\bar{\gamma}}\right)^2\right]. \tag{11}$$

Unlike the mean, this quantity depends on $\Delta\gamma$ and could be used as a probe of modular structure. We note, in particular, that a modular chain always exhibits a diffusion coefficient *greater than or equal to* that of its homoegeneous counterpart. However, this dependence appears in a term proportional to $e^{-b/2}\sinh(b/2)\tanh(b/2)$, thus its impact is most prominent for heavily biased walks and diminishes in the limit $b \to 0$. Expanding the full expression in powers of b, we would see $\Delta\gamma$ dependence only in terms of order-b^2 and higher. For an unbiased random walk, $b = 0$, this dependence disappears completely, and we have the familiar result that $\mathcal{C}_2 = 2k^*$. This may be compared to the large b limit, where

$$\mathcal{C}_2 \xrightarrow{b\to\infty} \left[1 + \frac{1}{4}\left(\frac{\Delta\gamma}{\bar{\gamma}}\right)^2\right]k^*. \tag{12}$$

Here varying $\Delta\gamma$ between zero and its maximum possible value of $2\bar{\gamma}$ can lead $\mathcal{C}_2$ to vary by a factor of 2.

To probe the behavior of $\mathcal{C}_2$ with varying bias in greater detail, we return to the exact expression given in Eq. (11) and note that at low b, $\frac{\partial \mathcal{C}_2}{\partial b} < 0$. However, on the condition that $\Delta\gamma/\bar{\gamma} > 2/\sqrt{3}$, there exists a value of b at which this derivative becomes positive. This leads $\mathcal{C}_2$ to increase with increasing b at sufficiently high values of b. This behavior, which is counter to the conventional understanding of the effect of bias, could serve as experimentally accessible evidence of underlying modular structure.

Our analytical results for $m_P = 2$ reveal that (1) the diffusion coefficient monotnonically grows with $\Delta\gamma$, and (2) for modular systems, it may display a nonmonotonic behavior with bias. These trends, as well as the enhancement of the diffusion coefficient with the lattice period m_P, are presented in Fig. 4 using numerical simulations.

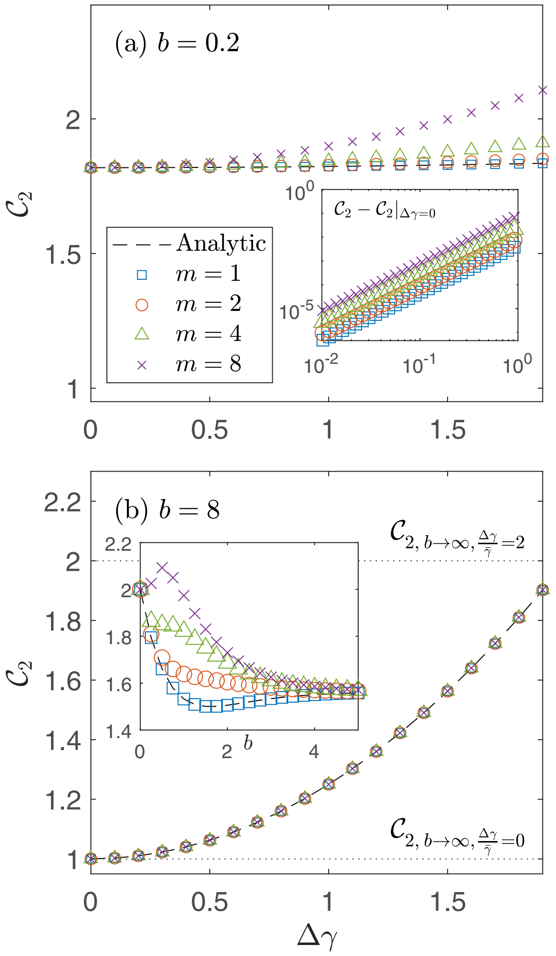

FIG. 4. Diffusion coefficient as a function of $\Delta\gamma$ for varying segment lengths, $m_A = m_B \equiv m$. Dashed black curves represent the analytic result for $m_P = 2$. Plots are shown for (a) low and (b) high bias. The inset of panel (a) depicts the same quantity on a log-log plot, with the $\Delta\gamma = 0$ contribution subtracted off, demonstrating that the diffusion coefficient scales quadratically with $\Delta\gamma$ for varying m. The inset of panel (b) shows $\mathcal{C}_2$ as a function of b for $\Delta\gamma = 1.5$, demonstrating its nonmonotinicity with increasing b at sufficiently high $\Delta\gamma/\bar{\gamma}$. Dotted lines in panel (b) represent the limits of $\mathcal{C}_2$ at high bias for the two extreme values of $\Delta\gamma$. These limits are based on the expressions of Sec. III A. $\tau = \bar{\gamma} = 1$.

3. *Skewness and kurtosis*

Taking the third-order derivative of the CGF with respect to χ we obtain the skewness, which is given by

$$\mathcal{C}_3 = 2\frac{\tau^2}{\bar{\gamma}}\frac{e^{-\frac{b}{2}}\sinh\left(\frac{b}{2}\right)}{\cosh^2\left(\frac{b}{2}\right)}\left[\cosh^2\left(\frac{b}{2}\right) + \frac{3}{4}\left(\frac{\Delta\gamma}{\bar{\gamma}}\right)^2 + \frac{3}{16}\sinh^2\left(\frac{b}{2}\right)\left(\frac{\Delta\gamma}{\bar{\gamma}}\right)^4\right]. \tag{13}$$

Like the first cumulant, this quantity vanishes completely in the absence of bias. However, $\Delta\gamma$ dependence is present in contributions that are first order in b. Therefore, at low but finite bias [Fig. 5(a)], the skewness may be said to express the modular structure of the chain more substantially than the diffusion coefficient does.

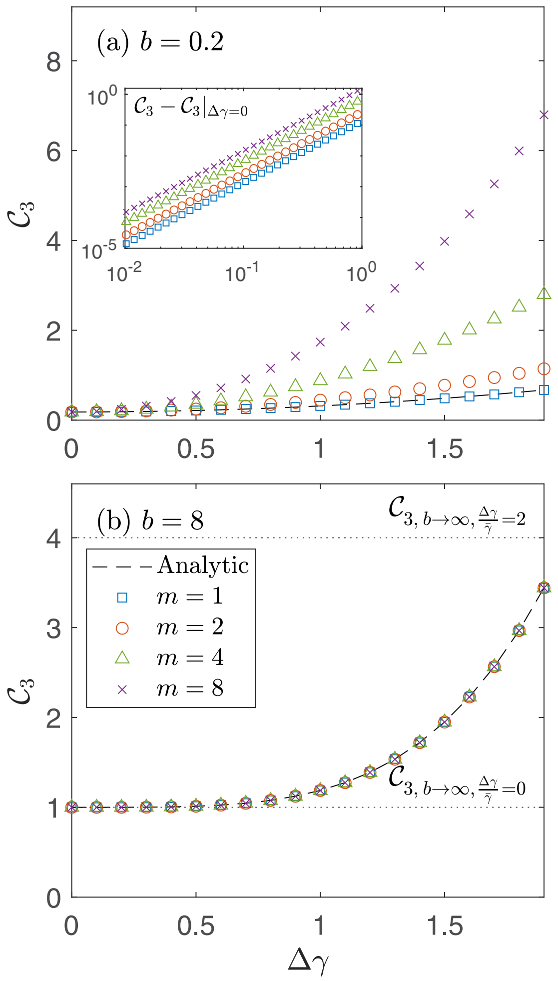

FIG. 5. Scaled skewness as a function of $\Delta\gamma$ for varying segment lengths, $m_A = m_B \equiv m$. Dashed black curves represent the analytic result for $m_P = 2$. Inset of panel (a): Log-log plot of the skewness with its value at $\Delta\gamma = 0$ subtracted off, showing that it scales quartically with $\Delta\gamma$ for varying m. Dotted lines in panel (b) represent the high-bias limits of $\mathcal{C}_3$ at the two extreme values of $\Delta\gamma$ for $m_A = m_B = 1$. Parameter values are the same as in Fig. 4.

In the opposite limit that $b \to \infty$, the skewness saturates to the finite value,

$$\mathcal{C}_3 \xrightarrow{b\to\infty} \left[1 + \frac{3}{16}\left(\frac{\Delta\gamma}{\bar\gamma}\right)^4\right]k^*; \tag{14}$$

see Fig. 5(b). This value exhibits fourth-order dependence on $\Delta\gamma$, in comparison to the second-order dependence of the diffusion coefficient on $\Delta\gamma$ in this regime. For very small $\Delta\gamma/\bar\gamma$, we expect the skewness to be less sensitive to the modular structure than the diffusion coefficient is.

Therefore, whether the diffusion coefficient or skewness better expresses underlying modular structure is dependent on the situation—if bias is high and the properties of the two regions are believed to differ only slightly, measurements of $\mathcal{C}_2$ are likely the more expressive option. If the bias is weak, the skewness is more sensitive to changes in $\Delta\gamma$ and will likely convey more about the structure. The skewness in the present model is positive for positive bias; it is interesting to devise related models that display skewness with the opposite sign to the bias [46].

The kurtosis is given by the fourth-order derivative of $\mathcal{G}(\chi)$ evaluated at $\chi = 0$,

$$\mathcal{C}_4 = 2\frac{\tau^2}{\bar\gamma}\frac{e^{-\frac{b}{2}}}{\cosh^3\left(\frac{b}{2}\right)}\left[\cosh^4\left(\frac{b}{2}\right) + f(b)\left(\frac{\Delta\gamma}{\bar\gamma}\right)^2 - g(b)\left(\frac{\Delta\gamma}{\bar\gamma}\right)^4 + \frac{15}{64}\sinh^4\left(\frac{b}{2}\right)\left(\frac{\Delta\gamma}{\bar\gamma}\right)^6\right], \tag{15}$$

where $f(b) = \frac{1}{64}(e^{-2b} - 36e^{-b} + 118 - 36e^{b} + e^{2b})$ and $g(b) = \frac{9}{256}(e^{-2b} - 12e^{-b} + 22 - 12e^{b} + e^{2b})$. Continuing the pattern that has emerged, we see more complex dependence on $\Delta\gamma$, now up to order $\Delta\gamma^6$.

Specifically, even at zero bias, the kurtosis exhibits $\Delta\gamma$ dependence, taking the form

$$\mathcal{C}_4 \xrightarrow{b\to 0} 2\left[1 + \frac{3}{4}\left(\frac{\Delta\gamma}{\bar\gamma}\right)^2\right]k^*. \tag{16}$$

This makes the kurtosis the lowest-order cumulant to be nonvanishing and express information about the modular structure even in the completely unbiased case.

In the infinite bias limit, the kurtosis goes to

$$\mathcal{C}_4 \xrightarrow{b\to\infty} \left[1 + \frac{1}{4}\left(\frac{\Delta\gamma}{\bar\gamma}\right)^2 - \frac{9}{16}\left(\frac{\Delta\gamma}{\bar\gamma}\right)^4 + \frac{15}{64}\left(\frac{\Delta\gamma}{\bar\gamma}\right)^6\right]k^*. \tag{17}$$

In sum, this analytical work and numerical simulations show that (1) the kurtosis grows with the degree of modularity $\Delta\gamma$ even at zero bias [Fig. 6(a)] and that (2) unlike the homogeneous case, in modular chains it can become negative [Fig. 6(b) and 6(c)].

We have shown that for the case where $m = 1$, varying amounts of information about the probability distribution over the quantity $n(t)/t$ at steady state are needed to discern underlying modular structure of the chain. The first cumulant, or mean velocity, is always identical to that for the analogous homogeneous chain. Therefore, at the very least, measurements of the second cumulant are needed to establish whether or not the transition rate alternates between two values, and, if so, the degree to which the values γ_A and γ_B differ. However, depending on the specific features of the random walk in question (i.e., if the bias is too low, or $\Delta\gamma/\bar\gamma$ is large), measurements of the skewness or kurtosis may be more effective.

B. Ratios of cumulants and the TUR

We note further that these expressions lend themselves to being studied in the context of their ratios. One such ratio is the Fano factor (relative fluctuations or "noise-to-signal" ratio). This quantity is known to be bounded in a manner dependent on the kinetic network structure [17]. Furthermore, it is significant to studies of the TUR, a cost-precision tradeoff which bounds it in terms of the entropy production rate [47–49], as well as the kinetic uncertainty relation, which bounds it in relation to the dynamical activity [50–52]. Evaluating the Fano factor for the modular random walk with $m_P = 2$, we note that prefactors on the expressions for the

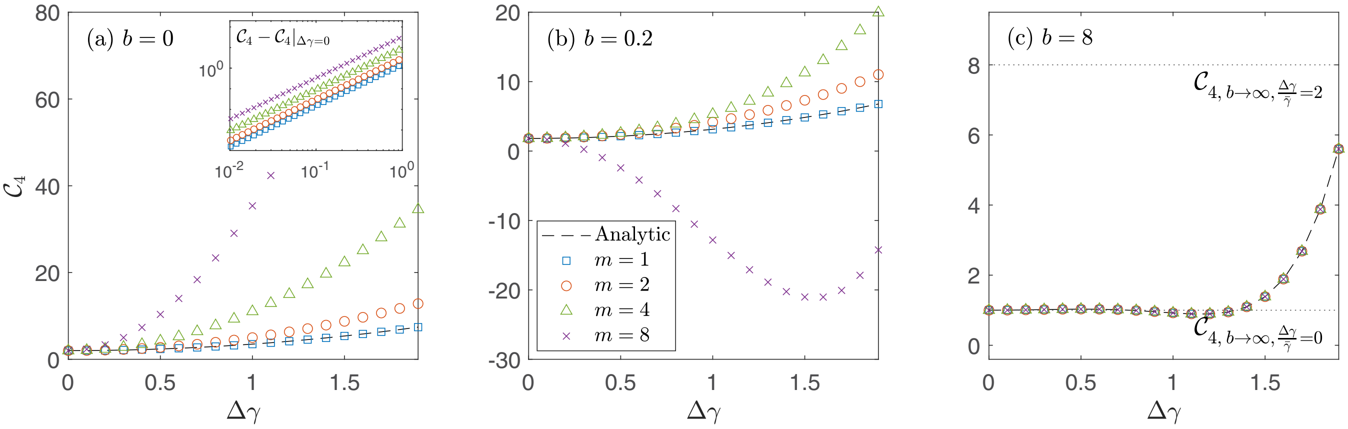

FIG. 6. Numerically determined scaled kurtosis as a function of $\Delta\gamma$ for varying $m_A = m_B \equiv m$ at (a) zero, (b) low, and (c) high bias. The black dashed curve represents the analytic expression determined for the $m_A = m_B = 1$ case. Inset of panel (a): Log-log plot of the kurtosis with its value at $\Delta\gamma = 0$ subtracted off, showing uniform scaling between different m values. Dotted lines in panel (c) represent the high-bias limits of $\mathcal{C}_4$ at low and high $\Delta\gamma$, as determined for $m_P = 2$ in Sec. III A. Parameter values are the same as in Fig. 4.

cumulants cancel out, leaving

$$\frac{\mathcal{C}_2}{\mathcal{C}_1} = \coth\left(\frac{b}{2}\right) + \frac{1}{4}\tanh\left(\frac{b}{2}\right)\left(\frac{\Delta\gamma}{\bar\gamma}\right)^2. \tag{18}$$

If we suppose the random walk to represent a physical system, with nonequilibrium conditions giving rise to the bias b, then it is consistent to suppose that the entropy production rate is given by $\langle\sigma\rangle = \mathcal{C}_1 b$. As such, this quantity itself expresses no more information about the network structure than does the mean velocity, $\mathcal{C}_1$, which we know exhibits no $\Delta\gamma$ dependence. This is in contrast to studies that have identified intimate links between entropy production rate and network structure when microscopic details are hidden, provided that a broad class of networks is considered [53,54].

We can, however, get an exact expression for the TUR ratio, $\langle\sigma\rangle\mathcal{C}_2/\mathcal{C}_1^2$, which is required to be greater than or equal to 2,

$$\langle\sigma\rangle\frac{\mathcal{C}_2}{\mathcal{C}_1^2} = b\frac{\mathcal{C}_2}{\mathcal{C}_1} = b\coth\left(\frac{b}{2}\right) + \frac{1}{4}b\tanh\left(\frac{b}{2}\right)\left(\frac{\Delta\gamma}{\bar\gamma}\right)^2. \tag{19}$$

This expression does indeed take on values greater than or equal to 2 for all values of b, going to exactly 2 strictly in the limit $b \to 0$. In addition, we note that the second term represents a nonnegative contribution present only in the case of a modular chain with nonzero bias. As such, a random walk on a modular chain never comes as close to saturating the TUR as its homogeneous counterpart in the presence of bias.

Turning to the higher-order cumulants, we note that the ratio $\mathcal{C}_4/\mathcal{C}_3$ exhibits the exact same behavior in the absence of modular structure. However, it exhibits a more complicated dependence on $\Delta\gamma$. For instance, if we focus on the regime where $\Delta\gamma$ is small compared to $\bar\gamma$, $\mathcal{C}_4/\mathcal{C}_3$ is given to good approximation by its expansion to second order in $\Delta\gamma/\bar\gamma$. Accordingly,

$$\frac{\mathcal{C}_4}{\mathcal{C}_3} = \coth\left(\frac{b}{2}\right)\left[1 + \frac{1}{\cosh^2\left(\frac{b}{2}\right)}\left(\frac{f(b)}{\cosh\left(\frac{b}{2}\right)} - \frac{3}{4}\right)\left(\frac{\Delta\gamma}{\bar\gamma}\right)^2\right] + O\left[\left(\frac{\Delta\gamma}{\bar\gamma}\right)^4\right]. \tag{20}$$

Unlike in the case of the relative fluctuations, the contribution from $\Delta\gamma/\bar\gamma$ takes on negative values at low, finite b. This means that modularity may suppress the ratio $\mathcal{C}_4/\mathcal{C}_3$ below the values it would take on in the homogeneous case, and even below $2/b$, distinguishing the behavior of this quantity from that of the standard TUR ratio.

In addition to the TUR, results derived in Ref. [27] pertaining to the statistics of the winding number (number of trips the system makes around a unicyclic network of states) place bounds on the ratios $\mathcal{C}_3/\mathcal{C}_1$ and $\mathcal{C}_4/\mathcal{C}_2$. The model considered here is a Markov jump process around a unicyclic network, thus satisfying the assumptions required for these results to hold.

C. Simulations

Simulations allow us to supplement our analytic results and go beyond the $m = 1$ case. We now elaborate on these results. We calculate the scaled cumulants for chains with greater segment lengths by implementing full counting statistics numerically.

In agreement with Ref. [31], simulations indicate that, for $m_A = m_B$, the expression derived analytically for the mean velocity, Eq. (10), holds independently of the segment length and $\Delta\gamma$. This is demonstrated in Fig. 3, where the markers indicating the numerically obtained values of the first cumulant line up with the analytic curve for *all* segment lengths throughout the range of bias values, with nonzero $\Delta\gamma$.

Beyond the mean, higher-order scaled cumulants do exhibit $\Delta\gamma$ dependence, even for the $m = 1$ case, as demonstrated in Sec. III A. Thus, we focus on plotting these quantities as a function of $\Delta\gamma$ to investigate how sensitively they express information about the structure of the chain, and how variation in the segment length impacts this behavior.

In general, simulations show that segment length has a substantial impact on the values and behavior of cumulants with $\Delta\gamma$, at low and intermediate bias. However, at high bias the cumulants no longer reflect a segment-size dependence, and they behave as they would in the case that segments were one-site long, but still *differently* from the analogous homogeneous random walk ($\Delta\gamma = 0$ point on the graph).

In particular, this is demonstrated for the diffusion coefficient in Fig. 4, where greater sensitivity to $\Delta\gamma$ is observed as the segment length increases, but only at low bias. Note that at zero bias (not depicted), simulations have shown that the diffusion coefficient goes to $2k^*$ for all $m_A = m_B$, as we showed analytically for $m_A = m_B = 1$, exhibiting no $\Delta\gamma$ dependence at any segment length.

The inset of Fig. 4(b) demonstrates the nonmonotonicity of $\mathcal{C}_2$ with increasing bias, discussed in Sec. III A. As shown, sufficiently high $\Delta\gamma/\bar{\gamma}$ leads the sign of $\partial\mathcal{C}_2/\partial b$ to change at a certain value of b. Interestingly, for the larger values of m probed only in simulations, the behavior is the reverse of that for $m = 1$, with $\mathcal{C}_2$ increasing at first, and then beginning to decrease with growing b at sufficiently high b. All curves converge in the high-b limit, as is consistent with the main plot.

The skewness, shown in Fig. 5, behaves similarly to the diffusion coefficient, taking on values that grow even more rapidly with increasing $\Delta\gamma$. Once again, the zero-bias case is not depicted, as the skewness is an odd-order cumulant and always vanishes in this regime.

Finally, the $\Delta\gamma$ dependence of the kurtosis is demonstrated in Fig. 6, including at zero bias. Away from the high-bias limit, variations in the segment length lead to substantial variations in the value of the kurtosis, including a strong nonmonotonic behavior of the kurtosis with $\Delta\gamma$ at intermediate bias.

While the higher-order cumulants take on different values for different segment lengths at low bias, we have demonstrated additionally that the nature of the scaling is consistent between different values of m. For instance, as we showed in Sec. III A, the diffusion coefficient for the $m = 1$ case scales quadratically with $\Delta\gamma$. Our simulations show that this scaling is quadratic for larger m as well, despite the form of the diffusion coefficient not matching exactly. This is demonstrated on the log-log plot in the inset of Fig. 4(a). Analogous findings for the skewness and kurtosis are shown in Figs. 5 and 6, respectively.

IV. REAL-SPACE SIMULATIONS OF THE MASTER EQUATION

Modular junctions under bias display rich, even nonmonotonic trends as a function of bias and $\Delta\gamma$, which we now aim to explain through direct simulations of the probability distribution functions. We obtain the PDF of the random walk by numerically solving the master equation for site populations at different times. As an initial condition, we assume a probability of 1 to be at site $n = 0$ and 0 elsewhere. We perform such simulations for long but finite chains ($\gtrsim 160$ sites) with absorbing boundary conditions. The simulation time is chosen long enough to observe a behavior corresponding to the steady-state limit of the associated finite cycle. That is, we reach the situation of only the smallest-magnitude eigenvalue in the Liouvillian substantially contributing to the dynamics. From the other end, simulation time is limited to ensure that boundary effects do not come into play.

We present the PDF for the random walk in Figs. 7 and 8 for the cases of low and high bias, respectively. In each case, we study the PDF at different times, and for four different values of the segment size m: 1, 2, 4, and 8.

As shown in Fig. 7, at low bias, while the mean of the distribution remains in the same position as that for the associated homogeneous chain, there are additional features that grow more dramatic with increasing segment length m. These features amount to a series of local maxima and minima arising as a result of the modular structure, and are understood to account for the exotic behavior of the higher-order cumulants.

In particular, population builds up in the leftmost sites of the "A" segments, characterized by slower rates. Due to these sites' positioning on the modular chain, population exits to the right at rate k_A, while it enters from the left at the faster rate k_B. In addition, the rate to exit to the left is suppressed by the factor e^{-b}. As such, population is generally fast to enter the A sites and slow to exit, accounting for the buildup of population at these sites observed in Fig. 7. Conversely, at the leftmost sites of "B" segments, we see a depletion of population due to the opposite effect. The transition rates into this state from A are relatively slow while the rate to exit to the left (towards A sites) is fast. A few examples of these population maxima and minima are labeled in Fig. 7(c) with the letters "A" and "B," respectively. Overall, we observe a probability distribution that deviates from the smooth curve exhibited by the homogeneous random walk. This deviation is more dramatic with longer segment lengths.

The limit of high bias is exemplified in Fig. 8, where we see similar buildup of population in the less rigid "A" segments and reduced population in the "B" segments due to the faster transitions out of these sites. The letters "A" and "B" label a few examples of this behavior in Fig. 8(c). However, some of the very complex structure observed in the lower bias case is absent, due to the fact that reverse transitions are effectively eliminated. A trajectory to reach site n is understood as simply a sequence of n steps forward, approximately half with waiting times characterized by the rate k_A and the other half by k_B. The order at which these steps occur is determined by the value of m, but this no longer impacts the higher-order cumulants of the distribution, explaining the indifference to m that the diffusion coefficient, skewness, and kurtosis were shown to exhibit at high bias in Sec. III C. The probability distribution for two different segment lengths values line up at values of n that are common multiples of the segment lengths.

In the Appendix, we calculate the cumulants from the real-space simulations of the PDF as a function of time. Finite time effects are rich [55,56]; in the steady state we show that the scaled cumulants agree with results from Sec. III.

V. SUMMARY

We have investigated the question of how the statistics of a random walk can be used to gain information about its underlying structure. Namely, we have examined random

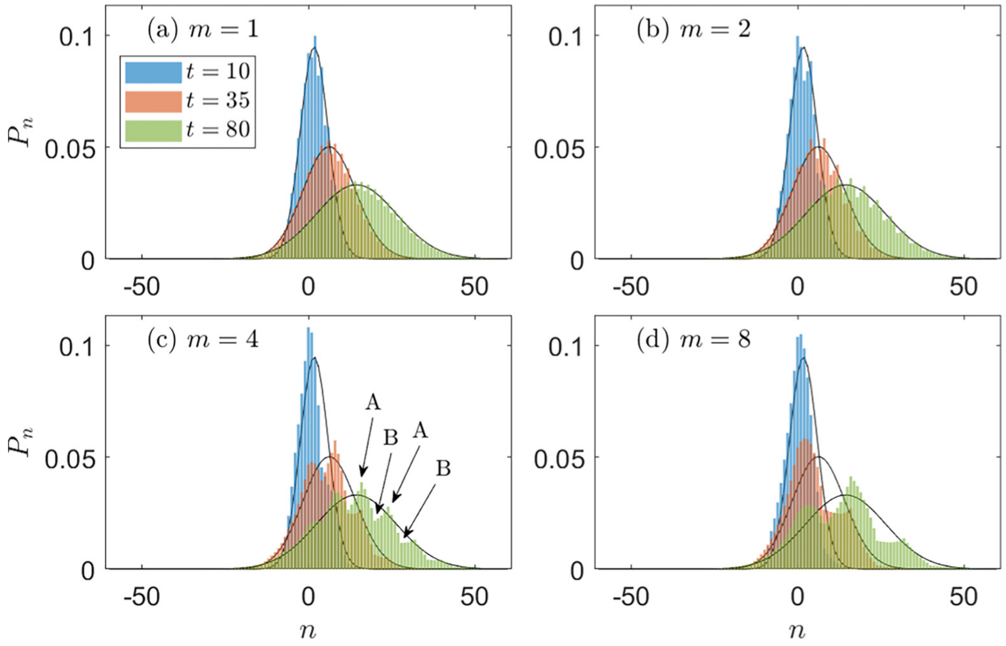

FIG. 7. Probability distribution functions at low bias obtained directly from the master equation for a 161-site chain. Each panel shows snapshots of the PDF at three different times for a given segment length, n. The black curves are the analogous probability distributions for the associated homogeneous random walk. $\bar{\gamma} = \Delta\gamma = \tau = 1$, $b = 0.2$.

walks on one-dimensional modular chains, with repeating fast and slow segments, by determining how the cumulants of the population distributions over their sites, scaled by time, behave in comparison to those for analogous homogeneous random walks. We have found that the first cumulant, or mean velocity, always takes a form in the long-time limit that matches the form for the homogeneous walk. Thus, measurements taking into account only the mean velocity at steady state are not sufficient to distinguish modular random walks from their homogeneous counterparts.

Studying the statistics in greater detail can, however, be an effective way to elucidate this very structure, with each

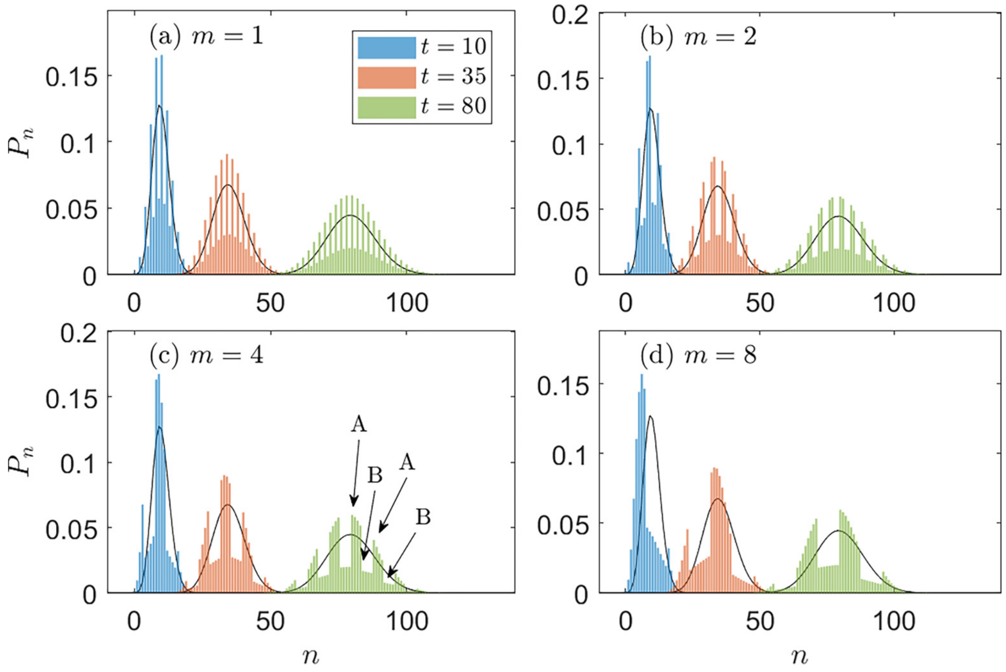

FIG. 8. Probability distribution functions at high bias obtained directly from the master equation for a 321-site chain (with most of the negative-n region not shown). Each panel shows snapshots of the PDF at three different times for a given segment length, n. The black curves are the analogous probability distributions for the associated homogeneous random walk. $b = 8$, representing the high-bias regime. Parameter values are otherwise the same as in Fig. 7.

of the higher-order cumulants discussed here reflecting the underlying modularity. This work probes cumulants as high as the kurtosis, which we found to be more expressive of modular structure than the diffusion coefficient and skewness; the kurtosis is nonzero, and it differs in value from that of its homogeneous counterpart even in the zero-bias case. In the presence of bias, however, all cumulants beyond the mean velocity can be used to gain information about the underlying structure.

Population distributions themselves can also elucidate the impact that modular structure has on the behavior of random walks. They exhibit deviations from the Gaussian form expected for homogeneous random walks, with local maxima and minima occurring with the same periodicity along the chain as the variations in transition rates. These are due to local buildup and depletion of population due to the differing transition rates within one period of the chain's structure.

The present work considered classical transport—it is interesting to generalize these observations to quantum dissipative transport, e.g., by using the formalism of quantum master equations with full counting statistics analysis [57,58]. In this regard it is intriguing to understand the role of quantum coherences in the behavior of noise going beyond the homogeneous case [59] and beyond the second moment. This task can be tackled by, e.g., the unified quantum master equation, [60–62], which was recently proved to be thermodynamically consistent in the steady-state regime [63,64].

Another avenue for further research would be to probe how the results derived here may extend to Langevin descriptions of particle diffusion in real space. Modular structure may then be reflected in the potential, for instance, with varying barrier heights between potential wells corresponding to the varying transition rates in our model.

Furthermore, the underlying structure of a random walk may not always be characterized by perfectly periodic variations in transition rates. Instead, one may consider a random walk on a disordered chain, with site-to-site transitions rates whose spatial variation is random. The analogous problem has been studied for Brownian motion in continuous space, with disorder having notable impacts on the diffusion coefficient [65,66]. Future work may investigate how this kind of underlying structure might be reflected in the higher-order cumulants of the population distribution for random walks.

In addition, it would be interesting to study how higher-order cumulants may reflect structure that is associated not just with transition rates, but also with the geometry of the network of states on which the random walk plays out. For instance, one may investigate how the presence of side chains or branches in the underlying network may be inferred through measurements of the statistics at steady state.

ACKNOWLEDGMENTS

D.S. acknowledges the NSERC discovery grant and the Canada Research Chairs Program. M.G. acknowledges support from the Ontario Graduate Scholarship and the NSERC Canada Graduate Scholarship-Doctoral. The authors acknowledge Anton Zilman for fruitful discussions on kinetic networks.

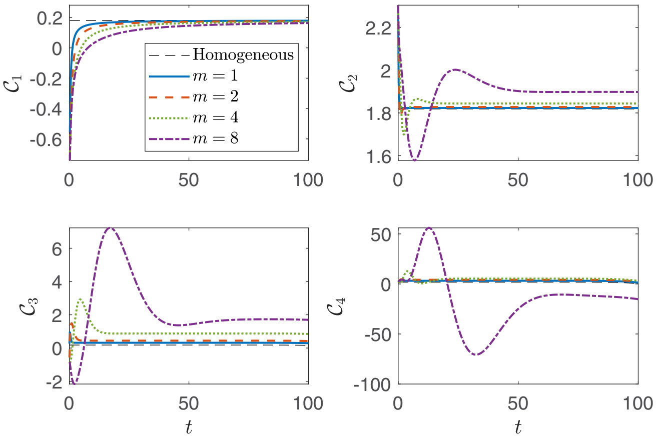

FIG. 9. The first four scaled cumulants as a function of time, calculated directly from the solution of the master equation for a 161-site chain. Different curves represent different segment lengths m, with the black dashed lines representing the steady-state value of each cumulant for the associated homogeneous chain. $b = 0.2$, representing the low-bias regime. $\tau = \bar{\gamma} = \Delta\gamma = 1$.

APPENDIX: CALCULATION OF THE CUMULANTS FROM REAL-SPACE SIMULATIONS

We use the numerical solutions of Sec. IV to calculate the scaled cumulants as a function of time. In particular, we calculate the moments of the distribution over $n(t)$, which are represented by single angle brackets,

$$\langle n^k(t)\rangle = \sum_n n^k P_n(t). \tag{A1}$$

The summation is done over the many sites included in the simulation. We then derive the scaled cumulants which are given by Eq. (3) in the long-time limit, but in the transient regime are time derivatives of functions of the moments:

$$\begin{aligned}
\mathcal{C}_1(t) &= \frac{d}{dt}\langle n(t)\rangle,\\
\mathcal{C}_2(t) &= \frac{d}{dt}\langle [n(t)-\langle n(t)\rangle]^2\rangle,\\
\mathcal{C}_3(t) &= \frac{d}{dt}\langle [n(t)-\langle n(t)\rangle]^3\rangle,\\
\mathcal{C}_4(t) &= \frac{d}{dt}[\langle [n(t)-\langle n(t)\rangle]^4\rangle - 3\langle [n(t)-\langle n(t)\rangle]^2\rangle^2].
\end{aligned} \tag{A2}$$

Calculation of these quantities involves taking time derivatives of the moments, given by

$$\frac{d}{dt}\langle n^k(t)\rangle = \sum_n n^k \frac{d}{dt}P_n(t) \tag{A3}$$

Note that the scaled cumulants here are time-dependent quantities that depend on the choice of initial state. In the long-time limit, they converge to the steady-state values calculated by the method outlined in Sec. III.

The scaled cumulants as calculated in this manner are shown in Figs. 9 and 10 for low bias ($b = 0.2$) and high bias ($b = 8$), respectively. The parameter values match those of Figs. 7 and 8 exactly. The probability distributions P_n for the 161- and 321-site chains do not exhibit a significant amount

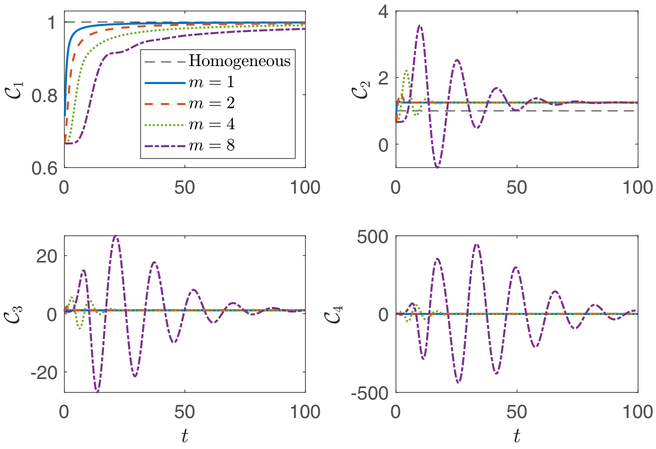

FIG. 10. The first four scaled cumulants as a function of time, for various segment lengths, calculated directly from the solution of the master equation for a 321-site chain. The black dashed lines represent the steady-state value of each cumulant for the associated homogeneous chain. This reference line is hidden in the plot of $\mathcal{C}_4$ due to the large amplitude of its pre-steady-state oscillations setting the vertical axis scale. $b = 8$, representing the high-bias regime. Parameter values are otherwise the same as in Fig. 9.

of population near the boundaries within the time frame of the simulation. As such, boundary effects may be ignored, and the simulations may be understood to approximate infinite random walks. However, these systems can be observed to reach a quasi-steady state as each of the scaled cumulants, $\mathcal{C}_k$, approaches its asymptotic value. The timescale for this to occur is the timescale for the analogous bipartite finite chain to reach its steady state, given by the largest nonzero eigenvalue of the rate matrix for this system, as discussed in Secs. II and III. This timescale is observed to grow substantially with the segment length m; in the context of the finite cycle, this is intuitive as a greater number of steps are needed for the population to spread out over all the states.

In addition, before reaching the quasi-steady state, we observe oscillations about the steady-state value of each scaled cumulant of second order and higher. These oscillations grow in magnitude with both bias and segment length. We attribute this behavior to the effects of population reaching different regions of the chain. Particularly in the high-bias case, the walker must traverse the initial, slower, "A" segment before reaching a faster, "B" segment. Thus, the diffusion coefficient peaks once a significant amount of population has reached the first "B" segment and had a chance to spread out more rapidly. Later, the diffusion coefficient decreases in value as population once again builds up in a slower "A" regions, etc. These oscillations die off once the population has spread out over enough of the spatial periods that each of these effects is effectively happening simultaneously. This takes longer to occur for longer segments.

The asymptotic values of the scaled cumulants line up with the steady-state values shown in Figs. 4–6 at $\Delta\gamma = 1$, with visible deviations from the value predicted for the homogeneous chain. Before reaching steady state, however, these quantities vary quite dramatically, particularly for larger m.

[1] R. Landauer, The noise is the signal, Nature (London) **392**, 658 (1998).

[2] N. G. van Kampen, *Stochastic Processes in Physics and Chemistry (Third Edition)*, (Elsevier, Amsterdam, 2007).

[3] G. Schaller, *Open Quantum Systems Far from Equilibrium*, (Springer International Publishing, Cham, 2014).

[4] G. T. Landi, M. J. Kewming, M. T. Mitchison, and P. P. Potts, Current fluctuations in open quantum systems: Bridging the gap between quantum continuous measurements and full counting statistics, arXiv:2303.04270 (2023).

[5] S. Iyer-Biswas and A. Zilman, First-passage processes in cellular biology, in *Advances in Chemical Physics*, edited by S. A. Rice and A. R. Dinner (Wiley, 2016).

[6] T. Schmiedl and U. Seifert, Stochastic thermodynamics of chemical reaction networks, J. Chem. Phys. **126**, 044101 (2007).

[7] R. Rao and M. Esposito, Nonequilibrium Thermodynamics of Chemical Reaction Networks: Wisdom from Stochastic Thermodynamics, Phys. Rev. X **6**, 041064 (2016).

[8] R. Rao and M. Esposito, Conservation laws and work fluctuation relations in chemical reaction networks, J. Chem. Phys. **149**, 245101 (2018).

[9] F. Avanzini and M. Esposito, Thermodynamics of concentration vs flux control in chemical reaction networks, J. Chem. Phys. **156**, 014116 (2022).

[10] X. Li and A. B. Kolomeisky, Mechanisms and topology determination of complex chemical and biological network systems from first-passage theoretical approach, J. Chem. Phys. **139**, 144106 (2013).

[11] A. Valleriani, X. Li, and A. B. Kolomeisky, Unveiling the hidden structure of complex stochastic biochemical networks, J. Chem. Phys. **140**, 064101 (2014).

[12] B. Punia, S. Chaudhury, and A. B. Kolomeisky, Understanding the reaction dynamics on heterogeneous catalysts using a simple stochastic approach, J. Phys. Chem. Lett. **12**, 11802 (2021).

[13] A. L. Thorneywork, J. Gladrow, Y. Qing, M. Rico-Pasto, F. Ritort, H. Bayley, A. B. Kolomeisky, and U. F. Keyser, Direct detection of molecular intermediates from first-passage times, Sci. Adv. **6**, 18 (2020).

[14] J. R. Moffitt and C. Bustamante, Extracting signal from noise: Kinetic mechanisms from a Michaelis–Menten-like expression for enzymatic fluctuations, FEBS J. **281**, 498 (2014).

[15] A. C. Barato and U. Seifert, Skewness and Kurtosis in Statistical Kinetics, Phys. Rev. Lett. **115**, 188103 (2015).

[16] T. Wampler and A. C. Barato, Skewness and kurtosis in stochastic thermodynamics, J. Phys. A: Math. Theor. **55**, 014002 (2022).

[17] P. Pietzonka, A. C. Barato, and U. Seifert, Universal bounds on current fluctuations, Phys. Rev. E **93**, 052145 (2016).

[18] P. Pietzonka, A. C. Barato, and U. Seifert, Affinity- and topology-dependent bound on current fluctuations, J. Phys. A: Math. Theor. **49**, 34LT01 (2016).

[19] Y. M. Blanter and M. Buttiker, Shot noise in mesoscopic conductors, Phys. Rep. **336**, 1 (2000).

[20] R. de Picciotto, M. Reznikov, M. Heiblum, V. Umansky, G. Bunin, and D. Mahalu, Direct observation of a fractional charge, Nature (London) **389**, 162 (1997).

[21] O. Zarchin, M. Zaffalon, M. Heiblum, D. Mahalu, and V. Umansky, Two-electron bunching in transport through a quantum dot induced by Kondo correlations, Phys. Rev. B **77**, 241303(R) (2008).

[22] O. Tal, M. Krieger, B. Leerink, and J. van Ruitenbeek, Electron-Vibration Interaction in Single-Molecule Junctions: From Contact to Tunneling Regimes, Phys. Rev. Lett. **100**, 196804 (2008).

[23] R. Ben-Zvi, R. Vardimon, T. Yelin, and O. Tal, Electron-vibration interaction in multichannel single-molecule junctions, ACS Nano **7**, 11147 (2013).

[24] A. Mu, O. Shein-Lumbroso, O. Tal, and D. Segal, Origin of the anomalous electronic shot noise in atomic-scale junctions, J. Phys. Chem. C **123**, 23853 (2019).

[25] B. K. Agarwalla and D. Segal, Assessing the validity of the thermodynamic uncertainty relation in quantum systems, Phys. Rev. B **98**, 155438 (2018).

[26] S. Saryal, H. Friedman, D. Segal, and B. K. Agarwalla, Thermodynamic uncertainty relation in thermal transport, Phys. Rev. E **100**, 042101 (2019).

[27] K. Ptaszyński, Bounds on skewness and kurtosis of steady-state currents, Phys. Rev. E **106**, 024119 (2022).

[28] F. Lai Liang and D. Segal, Long-range charge transport in homogeneous and alternating-rigidity chains, J. Chem. Phys. **157**, 104106 (2022).

[29] R. Korol, M. Kilgour, and D. Segal, ProbeZT: Simulation of transport coefficients of molecular electronic junctions under environmental effects using Buttiker's probes, Comput. Phys. Commun. **224**, 396 (2018).

[30] W. Dieterich, I. Peschel, and W. R. Schneider, Diffusion in periodic potentials, Z. Phys. B **27**, 177 (1977).

[31] B. Derrida, Velocity and diffusion constant of a periodic one-dimensional hopping model, J. Stat. Phys. **31**, 433 (1983).

[32] A. Di Crescenzo, C. Macci, and B. Martinucci, Asymptotic results for random walks in continuous time with alternating rates, J. Stat. Phys. **154**, 1352 (2014).

[33] P. Reimann, C. Van den Broeck, H. Linke, P. Hänggi, J. M. Rubi, and A. Pérez-Madrid, Giant Acceleration of Free Diffusion by Use of Tilted Periodic Potentials, Phys. Rev. Lett. **87**, 010602 (2001).

[34] P. Reimann and R. Eichhorn, Weak Disorder Strongly Improves the Selective Enhancement of Diffusion in a Tilted Periodic Potential, Phys. Rev. Lett. **101**, 180601 (2008).

[35] L. F. Perondi and P.-M. Binder, Tracer diffusion in small periodic systems, Phys. Rev. B **47**, 14221 (1993).

[36] P. Illien, O. Bénichou, G. Oshanin, A. Sarracino, and R. Voituriez, Nonequilibrium Fluctuations and Enhanced Diffusion of a Driven Particle in a Dense Environment, Phys. Rev. Lett. **120**, 200606 (2018).

[37] W. A. M. Morgado and S. M. D. Queirós, Thermostatistics of small nonlinear systems: Poissonian athermal bath, Phys. Rev. E **93**, 012121 (2016).

[38] L. Defaveri, E. Barkai, and D. A. Kessler, Brownian particles in periodic potentials: Coarse-graining versus fine structure, Phys. Rev. E **107**, 024122 (2023).

[39] D. R. Bond and D. R. Lovley, Electricity production by *Geobacter sulfurreducens* attached to electrodes, Appl. Environ. Microbiol. **69**, 1548 (2003).

[40] D. R. Lovley and D. J. F. Walker, *Geobacter* protein nanowires, Front. Microbiol. **10**, 2078 (2019).

[41] X. Ru, P. Zhang, and D. N. Beratan, Assessing possible mechanisms of micrometer-scale electron transfer in heme-free *Geobacter sulfurreducens* Pili, J. Phys. Chem. B **123**, 5035 (2019).

[42] J. C. Genereux and J. K. Barton, Mechanisms for DNA charge transport, Chem. Rev. **110**, 1642 (2010).

[43] D. Segal, A. Nitzan, W. B. Davis, M. R. Wasielewsky, and M. A. Ratner, Electron transfer rates in bridged molecular systems: A steady state analysis of coherent tunneling and thermal transitions, J. Phys. Chem. B **104**, 3817 (2000).

[44] J. M. Moix, M. Khasin, and J. Cao, Coherent quantum transport in disordered systems: I. The influence of dephasing on the transport properties and absorption spectra on one-dimensional systems, New J. Phys. **15**, 085010 (2013).

[45] D. Segal, Current fluctuations in quantum absorption refrigerators, Phys. Rev. E **97**, 052145 (2018).

[46] D. S. P. Salazar, Thermodynamic skewness relation from detailed fluctuation theorem, Phys. Rev. E **106**, L042101 (2022).

[47] A. C. Barato and U. Seifert, Thermodynamic Uncertainty Relation for Biomolecular Processes, Phys. Rev. Lett. **114**, 158101 (2015).

[48] T. R. Gingrich, J. M. Horowitz, N. Perunov, and J. L. England, Dissipation Bounds All Steady-State Current Fluctuations, Phys. Rev. Lett. **116**, 120601 (2016).

[49] J. P. Garrahan, Simple bounds on fluctuations and uncertainty relations for first-passage times of counting observables, Phys. Rev. E **95**, 032134 (2017).

[50] I. D. Terlizzi and M. Baiesi, Kinetic uncertainty relation, J. Phys. A: Math. Theor. **52**, 02LT03 (2018).

[51] X. He, P. Pakkiam, A. A. Gangat, M. J. Kewming, G. J. Milburn, and A. Fedorov, Quantum clock precision studied with a superconducting circuit, arXiv:2207.11043 (2022).

[52] V. T. Vo, T. V. Vu, and Y. Hasegawa, Unified thermodynamic–kinetic uncertainty relation, J. Phys. A: Math. Theor. **55**, 405004 (2022).

[53] D. J. Skinner and J. Dunkel, Improved bounds on entropy production in living systems, Proc. Natl. Acad. Sci. USA **118**, e2024300118 (2021).

[54] D. J. Skinner and J. Dunkel, Estimating Entropy Production from Waiting Time Distributions, Phys. Rev. Lett. **127**, 198101 (2021).

[55] S. K. Manikandan, S. Ghosh, A. Kundu, B. Das, V. Agrawal, D. Mitra, A. Banerjee, and S. Krishnamurthy, Quantitative analysis of nonequilibrium systems from short-time experimental data, Commun. Phys. **4**, 258 (2021).

[56] S. K. Manikandan, B. Das, A. Kundu, R. Dey, A. Banerjee, and S. Krishnamurthy, Nonmonotonic skewness of currents in nonequilibrium steady states, Phys. Rev. Res. **4**, 043067 (2022).

[57] M. Esposito, U. Harbola, and S. Mukamel, Nonequilibrium fluctuations, fluctuation theorems, and counting statistics in quantum systems, Rev. Mod. Phys. **81**, 1665 (2009).

[58] H. M. Friedman, B. K. Agarwalla, and D. Segal, Quantum energy exchange and refrigeration: A full-counting statistics approach, New J. Phys. **20**, 083026 (2018).

[59] M. Esposito and P. Gaspard, Exactly solvable model of quantum diffusion, J. Stat. Phys. **121**, 463 (2005).

[60] A. Trushechkin, Unified Gorini-Kossakowski-Lindblad-Sudarshan quantum master equation beyond the secular approximation, Phys. Rev. A **103**, 062226 (2021).

[61] P. P. Potts, A. A. S. Kalaee, and A. Wacker, A thermodynamically consistent Markovian master equation beyond the secular approximation, New J. Phys. **23**, 123013 (2021).

[62] G. McCauley, B. Cruikshank, D. I. Bondar, and K. Jacobs, Accurate Lindblad-form master equation for weakly damped quantum systems across all regimes, npj Quantum Inf. **6**, 74 (2020).

[63] M. Gerry and D. Segal, Full counting statistics and coherences: Fluctuation symmetry in heat transport with the unified quantum master equation, Phys. Rev. E **107**, 054115 (2023).

[64] A. Soret, V. Cavina, and M. Esposito, Thermodynamic consistency of quantum master equations, Phys. Rev. A **106**, 062209 (2022).

[65] M. Khoury, A. M. Lacasta, J. M. Sancho, and K. Lindenberg, Weak Disorder: Anomalous Transport and Diffusion Are Normal Yet Again, Phys. Rev. Lett. **106**, 090602 (2011).

[66] M. S. Simon, J. M. Sancho, and K. Lindenberg, Transport and diffusion of overdamped Brownian particles in random potentials, Phys. Rev. E **88**, 062105 (2013).